A trade-off between ligand and strain effects optimizes the oxygen reduction activity of Pt alloys

Regina M. Kluge,[†a,*] Richard W. Haid,[†a] Alexander Riss,[b] Yang Bao,[b] Knud Seufert,[b] Thorsten O. Schmidt,[a] Sebastian A. Watzele,[a] Johannes V. Barth,[b] Francesco Allegretti,[b] Willi Auwärter,[b] Federico Calle-Vallejo,[c,d,e,*] and Aliaksandr S. Bandarenka[a,f,*]

To optimize the performance of catalytic materials, it is paramount to elucidate the dependence of the chemical reactivity on the atomic arrangement of the catalyst surface. Therefore, identifying the nature of the active sites that provide optimal binding of reaction intermediates is the first step toward a rational catalyst design. In this work, we focus on the oxygen reduction reaction (ORR), an essential constituent of several energy provision and storage devices. Among the state-of-the-art ORR catalysts are platinum (Pt) and its alloys. The latter benefit from the so-called ligand and strain effects, which influence the electronic properties of the surface. Here, we "visualize" the active sites on $Pt_3Ni(111)$ in an acidic medium with a lateral resolution in the nanometer regime via an in-situ technique based on electrochemical scanning tunnelling microscopy. In contrast to pure Pt, where the active sites are located at concave sites close to steps, $Pt_3Ni(111)$ terraces contain the most active centres, while steps show activity to a comparable or lesser extent. We confirm the experimental findings by a model based on alloy- and strain-sensitive generalized coordination numbers. With this model, we are also able to assess both the composition and the geometric configuration of optimal catalytic active sites on various Pt alloy catalysts. In general, the interplay of ligand effects and lattice compression resulting from the alloying of Pt with 3d transition metals (Ti, Co, Ni, Cu) gradually increases the generalized coordination number of surface Pt atoms, thereby making (111) terraces highly active. This combination of theoretical and experimental tools provides clear strategies to design more efficient Pt alloy electrocatalysts for oxygen reduction.

Introduction

On the route to an eco-conscious provision and storage of energy, electrochemical devices such as hydrogen fuel cells and metal-air batteries are among the key technologies.[1,2,3] Despite their great promise, numerous electrochemical technologies are currently not efficient enough to be massively commercialized and their optimization has proved incredibly challenging.[4,5] In fact, the growing consensus is that their optimization requires an in-depth understanding of the electrochemical processes at the electrified solid/liquid interfaces. In-situ and operando techniques together with computational modelling are most suitable to assess the nature of the active sites.

A stumbling block for hydrogen fuel cells and metal-air batteries is the sluggish kinetics of the oxygen reduction reaction (ORR in acidic medium: $O_2 + 4H^+ + 4e^- \leftrightarrow 2H_2O$). Currently, the state-of-the-art ORR catalysts are mainly based on platinum (Pt). For

a. Physik-Department ECS, Technische Universität München, James-Franck-Straße 1, 85748 Garching, Germany.

b. Physik-Department E20, Technische Universität München, James-Franck-Straße 1, 85748 Garching, Germany.

c. Nano–Bio Spectroscopy Group and European Theoretical Spectroscopy Facility (ETSF), Department of Polymers and Advanced Materials: Physics, Chemistry and Technology, University of the Basque Country UPV/EHU, Avenida Tolosa 72, 20018 San Sebastián, Spain.

d. IKERBASQUE, Basque Foundation for Science, Plaza de Euskadi 5, 48009 Bilbao, Spain.

e. Department of Materials Science and Chemical Physics & Institute of Theoretical and Computational Chemistry (IQTCUB), University of Barcelona, Martí i Franquès 1, 08028 Barcelona, Spain.

f. Catalysis Research Center TUM, Ernst-Otto-Fischer-Straße 1, 85748 Garching, Germany.

* Corresponding authors' e-mails:
(R. M. K.) regina.kluge@ph.tum.de
(F. C.-V.) federico.calle@ehu.es
(A. S. B.) bandarenka@ph.tum.de
† Equally contributing first authors.

the past two decades, trends in the catalytic activity of surface sites have often been extracted from activity measurements on well-defined crystal planes and computational models hinging on the Sabatier principle.[6,7,8,9] For pure Pt, measurements on stepped single-crystal surfaces[10,11] indicated highly-coordinated sites in the vicinity of undercoordinated sites as the most active for the ORR.[12,13,14] These results are in line with the high activity of concave Pt nanoparticles.[15,16,17,18,19] Both experimental and computational results have consistently shown that Pt(111) does not offer optimal binding conditions for adsorbed hydroxyl and hydroperoxyl intermediates (*OH and *OOH).[4] In fact, an optimal ORR catalyst should bind *OH around 0.1-0.15 eV more weakly than Pt(111).[4,12,20,21,22]

A common approach to weaken the binding energy of the ORR intermediates is the alloying of Pt with early (e.g. Sc, Y) or late (e.g. Fe, Co, Ni, Cu) transition metals (M).[20,23,24,25,26,27] Inspired by the discovery of the exceptional ORR activity of $Pt_3Ni(111)$ in acidic medium,[15] several groups have synthesized Pt_xNi nanoparticles with high performance.[28,29,30,31] The type and amount of alloying material have a considerable impact on the ORR activity (a detailed summary is given in reference 32). The improved performance of Pt alloy catalysts compared to pure Pt is often explained by the presence of so-called ligand and strain effects. Ligand effects arise from the combination of Pt atoms with dissimilar neighbouring atoms, which influence their electronic structure and adsorption behaviour.[33,34] Strain effects originate from different interatomic distances at the surface compared to the bulk of pure Pt.[35,36,37]

Although it is widely accepted that ligand and strain effects play a key role in the superior ORR performance of Pt alloys, the nature of their active sites remains elusive. A plausible strategy to fill this void is the combination of an in-situ technique together with computational modelling to assess the conditions for optimal performance. As the experimental approach, we chose electrochemical scanning tunnelling microscopy (EC-STM) under reaction conditions as it can map the electrode surface with a resolution down to the nanometre or even atomic scale while at the same time allowing potential control. The method can identify active sites by noise features in the EC-STM signal.[13,14,38,39,40,41,42] By introducing a reaction at the electrode/electrolyte interface, the tunnelling barrier experiences spatial and time-dependent changes. Since the tunnelling barrier and its properties mainly govern the recorded STM signal and its stability, the noise arising under these conditions can be interpreted as a perturbation induced by a catalytic event.[41] In short, an increase in the noise level of the STM signal indicates the presence of active sites and can even reveal quantitative information about the local activity.[14,41] To illustrate the abilities of the "noise"-EC-STM (hereon referred to as n-EC-STM) technique for the investigation of Pt alloys under ORR conditions, we used the high-performing model system $Pt_3Ni(111)$ in an acidic medium. Here, we find (111) terraces as the most active sites for the ORR. Furthermore, we observe sites of different coordination, such as step sites with either slightly inferior or comparable activity to the (111) terrace sites. In order to support the experimental data and extend our conclusions to other alloys, a computational model based on alloy-sensitive generalized coordination numbers was elaborated. According to this model, both "overcoordinated" and "undercoordinated" defects lower the activity on $Pt_3Ni(111)$ terraces, in line with our experimental observations. The strength of the model is to quantify strain and ligand effects in simple geometric terms and outline the strain-composition-coordination conditions for optimal binding. To test the predictive power of the model, the approach based on alloy-sensitive generalized coordination numbers is extended to a broader range of alloys, e.g., to Pt_3M bulk alloys (M = Ti, Co, Cu) and PtCu near-surface alloys and compared to experiments.

Since the findings on the alloy materials deviate substantially from the case of pure Pt(111), we observe that to give rational directions for optimal ORR electrocatalysts, it is vital to combine experimental in-situ scanning probe techniques and computational models involving morphology- and composition-sensitive descriptors.

Methods

Experimental Details

Sample Preparation. Prior to the electrochemical measurements, the $Pt_3Ni(111)$ single-crystal disk electrode (Ø 5 mm, MaTecK) was repeatedly sputter-cleaned under ultra-high vacuum (UHV) conditions using an Ar^+-beam of 10 µA ion current and 1 kV voltage. It was annealed for 10 min after each sputtering step, and the temperature was stepwise increased up to 1050 K. After the last annealing step, the sample was slowly cooled down to room temperature.

LEED. A commercial low-energy electron diffraction (LEED) apparatus (SPECTALEED, Omicron NanoTechnology GmbH) was employed to assess the quality of the surface order in a dedicated UHV chamber operating at a base pressure of ≈ 3 x 10^{-10} mbar. The chamber contains all the necessary facilities for surface cleaning and sample preparation. Some artefacts in the LEED patterns arising from a deterioration of the fluorescent screen were removed by computer software for ease of inspection.

LT-STM. Low-temperature scanning tunnelling microscopy (LT-STM) experiments were performed using a CreaTec instrument under UHV conditions (p ≈ 10^{-10} mbar) at a temperature of 6 K. The sample was prepared by cycles of argon ion sputtering (at 1 kV) and annealing at a maximal temperature of 1050 K. For selected preparations, CO was dosed onto the surface to aid tip formation. Images were recorded in the constant-current mode; the respective imaging parameters are given in the figure captions. The images were subjected to standard corrections, i.e., plane-subtraction, global brightness/contrast adjustments, and fast Fourier transformation (FFT) filtering using the Nanonis image viewer software and the WSxM software[43].

Electrochemical Measurements. The quality of the crystal was probed by performing cyclic voltammetry (CV) experiments in Ar-saturated (Argon 5.0, Westfalen, Germany) electrolytes at 50 mV s^{-1} scan rate. To study the ORR electrocatalytic activity,[44] rotating disk electrode (RDE) (Pine Instrument Company, USA) experiments were performed in O_2-saturated (Oxygen 4.5, Linde, Germany) solutions at 1600 rpm rotational speed and 50 mV s^{-1} scan rate. Results were iR-corrected for the electrolyte resistance obtained from electrochemical impedance spectroscopy (EIS) measurements. The experiments were performed with a BioLogic VSP-300 potentiostat (BioLogic, France). The electrolyte was 0.1 M perchloric acid ($HClO_4$, Suprapur, Merck, Germany). The potentials were recorded either against a mercury-mercurous sulphate electrode (MMS, SI Analytics, Germany) or a reversible hydrogen electrode (RHE, HydroFlex®, gaskatel, Germany). The potential values (U) are calibrated against each other via: $U_{RHE} = U_{MMS} + 0.66$ V + 0.059 V * pH. The reference electrode is indicated in the indices. The electrochemical setup was completed by a Pt wire counter electrode (99.9%, Goodfellow, Germany). The cell was regularly cleaned with "Caro's acid", i.e., a 3:1 ratio of H_2SO_4 (96%, Roth) and H_2O_2 (30%, Roth) and subsequently rinsed with boiling ultrapure water multiple times.

n-EC-STM. All EC-STM experiments were performed using a MultiMode EC-STM/EC-AFM scanning probe microscope (Veeco Instruments) connected to a NanoScope III scan feedback controller and a Universal Bipotentiostat (Veeco Instruments). The STM tips were mechanically ripped from a $Pt_{80}Ir_{20}$ wire (GoodFellow, Ø 0.25 mm) and subsequently isolated using Apiezon wax.[45] The crystal was clamped between a homemade stainless steel sample holder and a polytetrafluoroethylene (PTFE) ring. The PTFE ring exposed a sample area of 0.126 cm^2 to the electrolyte. The reference and counter electrodes (Pt wires, MaTecK, Ø 0.5 mm, 99.99 % purity) were immersed in the electrolyte next to the STM tip. Due to the small dimensions of the electrochemical cell in the STM setup, a Pt wire as a quasi-reference electrode was required. Even though a direct transfer into, e.g., RHE-scale is not possible, its use has proven reliable for n-EC-STM measurements.[13,14,38] All measurements were conducted at room temperature with the electrolyte exposed to air. More details on the methodology of the n-EC-STM method can be found in reference 13, in the results and discussion section of the main text of this article, and in section S3 of the Supplementary Information (SI).

**Density Functional Theory (DFT) Calculations**

The spin-unrestricted DFT calculations were made with the Vienna ab initio simulation package (VASP)[46] using the Perdew-Burke-Ernzerhof (PBE) exchange-correlation functional[47] and the projector augmented-wave (PAW) method.[48] The (111) surfaces of the Pt_3M (M = Ni, Ti, Co, Cu) bulk alloys, and PtCu near-surface alloys (NSAs) were modelled with 2×2 supercells, whereas the (533) and (221) surfaces were modelled with 2×1 supercells. These supercells are large enough to avoid artificial lateral interactions between the adsorbates. For instance, the difference in the adsorption energy of *OH between the 2×2 (111) cell we used and a 3×3 (111) cell is only 0.01 eV for pure Pt. All slab models contained four metal layers and were modelled based on lattice constants of 3.98, 3.90, 3.88, 3.89, and 3.95 Å for PtCu NSAs, Pt_3Cu, Pt_3Ni, Pt_3Co, and Pt_3Ti, respectively. The two topmost surface layers and the adsorbates were allowed to relax in all directions, whereas the bottommost layers were fixed at the bulk equilibrium positions. We used a plane-wave cut-off of 450 eV, k_BT = 0.2 eV and subsequent extrapolation of the total energies to 0 K, and the conjugate-gradient optimization scheme until the maximal force on any atom was less than 0.05 eV $Å^{-1}$. Monkhorst-Pack meshes[49] of 6×6×1, 6×3×1 and 6×4×1 for the (111), (533) and (221) facets ensured the convergence of the adsorption energies within 0.05 eV. (111) terraces were used to emulate experimental terrace sites, while (533) and (221) slabs (with (100) and (111) defects, respectively) were used to emulate areas around steps. Both facets have long enough terraces of 4 atoms with converged generalized coordination numbers for step-edge, terrace and bottom sites. The adsorption sites are illustrated in Figure S9. The vacuum layer between periodically repeated images in the vertical direction was larger than 14 Å and dipole corrections were applied. The data for pure Pt were taken from previous studies.[50] H_2O and H_2 were calculated by sampling the Γ-point only in cells of 15 Å × 15 Å × 15 Å and using k_BT = 0.001 eV. The computational hydrogen electrode (CHE) was used to describe the energetics of proton-electron pairs.[6] We modelled the ORR via an associative pathway, in which O_2 is sequentially transformed into *OOH, *O, *OH, and H_2O,[6] see section S5.1 in the SI. The free energies were approximated as $\Delta G \approx \Delta E_{DFT} + \Delta ZPE - T\Delta S + \Delta E_{solvation}$, where ΔE_{DFT} is the DFT-calculated energy of reaction, ΔZPE is the zero-point energy change (calculated also with DFT making use of the harmonic oscillator approximation), and $T\Delta S$ is the entropy change at 298.15 K. As customary for ORR models based on the CHE, ΔS includes no entropy for the adsorbates and all the contributions for H_2 and H_2O.[36] Solvent-adsorbate interactions were incorporated as an external correction depending on the adsorbate and the alloy.[51] The assessment of generalized coordination numbers, activity enhancements, specific values of the gas-phase, liquid-phase, and solvent-adsorbate stabilization corrections, together with the adsorption free energies and the converged Cartesian coordinates, can be found in the SI, section S5.

Results and Discussion

In the following, we will provide a comprehensive approach consisting of high-resolution, in-situ experiments combined with DFT calculations to elucidate active sites on Pt alloy catalysts for the ORR. We will use the experimental technique on the $Pt_3Ni(111)$ surface, which is state-of-the-art for ORR catalysis. In order to assure a well-defined model system the $Pt_3Ni(111)$ single-crystal surface was characterized using surface science and electrochemical techniques. Figure 1a shows a typical LEED pattern imaged on the fluorescent screen. From the hexagonal arrangement of the diffraction spots, the (111) orientation of the surface is confirmed, with no evidence of reconstructions altering the surface periodicity.[21,52] In addition, Figure 1b recounts a typical LT-STM measurement on the surface of the freshly prepared crystal, where the (111) surface can be distinguished with atomic resolution. High-symmetry directions are marked in the image. Additional images are included in Figure S1. As a rough estimate, the Pt-Pt interatomic distance was extracted from these images as 2.61 ± 0.07 Å. We note that the error accounts only for the statistical deviation between the different LT-STM images made on $Pt_3Ni(111)$. In addition, systematic error sources can lead to a larger deviation, which is not included in the error given here. More details on the determination of the lattice constant and the consideration of errors are given in section S1 of the SI.

Assuming a literature value of 2.77 Å for Pt(111),[50] the decrease of the $Pt_3Ni(111)$ lattice constant compared to the unstrained Pt(111) surface is 5.8 ± 2.5 %. Given this substantial amount of compression, strain effects are bound to play a crucial role in ORR electrocatalysis.

The electrochemical performance of the $Pt_3Ni(111)$ surfaces was tested in 0.1 M $HClO_4$. The voltammetric curve shown in Figure 1c is in agreement with the literature, where the typical peaks attributed to surface oxidation and reduction are present. At potentials lower than ca. 0.3 V_{RHE}, the features can be attributed to the ad-/desorption of hydrogen, whereas the features at around 0.8 V_{RHE} can be assigned to OH ad/desorption.[15,53] The ORR performance (Figure 1d) was evaluated in RDE experiments, and a specific ORR activity of 7.6 mA cm^{-2} (normalised to geometric area) was obtained at 0.9 V_{RHE}. This is slightly higher than the activity reported at room temperature in previous works.[53] Table S1 provides a detailed comparison of ORR activities and shows that the $Pt_3Ni(111)$ surface is the most active among PtM (M=Ni, Co, Cu) alloys of various crystal orientations. In the past, it was observed that a pure Pt layer forms on the surface of a PtM bulk after electrochemical cycling in acidic media. The compressive strain introduced thereby on the Pt surface leads to a downshift of the d-band centre,[15] weaker average binding of the ORR intermediates to the surface,[54,55,56] and better ORR performance. The dissolution of the other transition metal atom in the alloy (known as de-alloying) can indeed induce significant changes in the activity of numerous Pt alloys, as recently reported.[57]
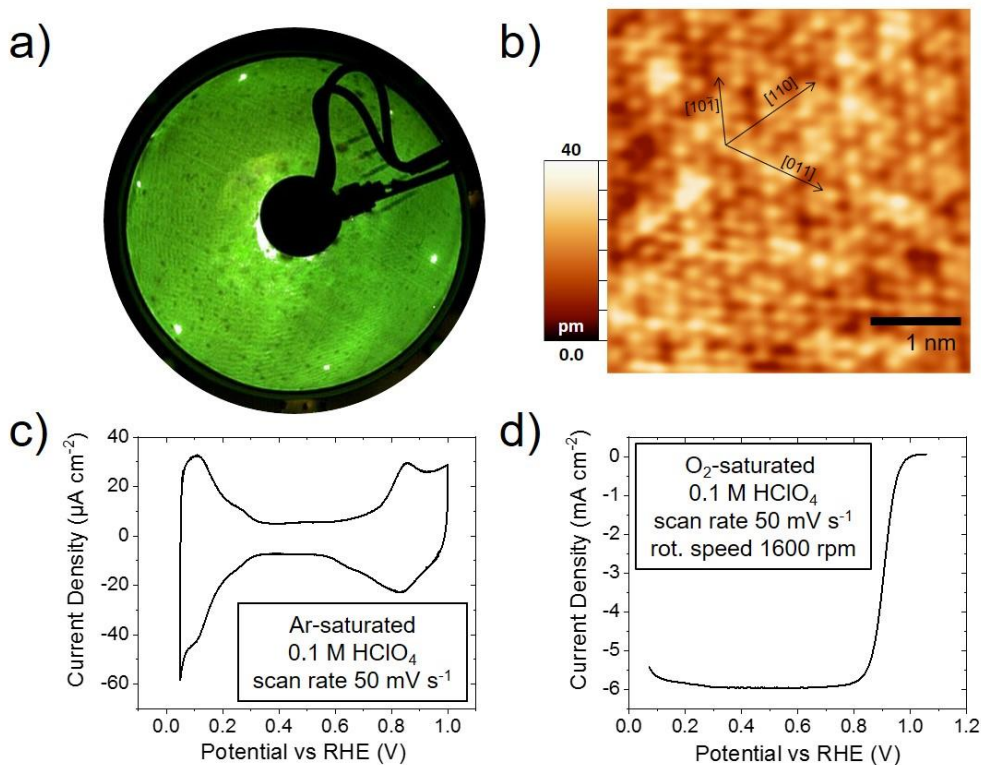
Figure 1. Surface science and electrochemical investigation of the freshly prepared $Pt_3Ni(111)$ surface. a) LEED image at a primary electron energy of 73 eV. b) High-resolution LT-STM image confirming the (111) orientation (tip-sample bias: -10 mV; tip set-point: 3.0 nA). c) CV in Ar-saturated 0.1 M $HClO_4$ at a scan rate of 50 mV s^{-1}. d) Anodic scan of the polarization curve in O_2-saturated 0.1 M $HClO_4$ recorded at 1600 rpm and a scan rate of 50 mV s^{-1}, 85% iR-corrected.
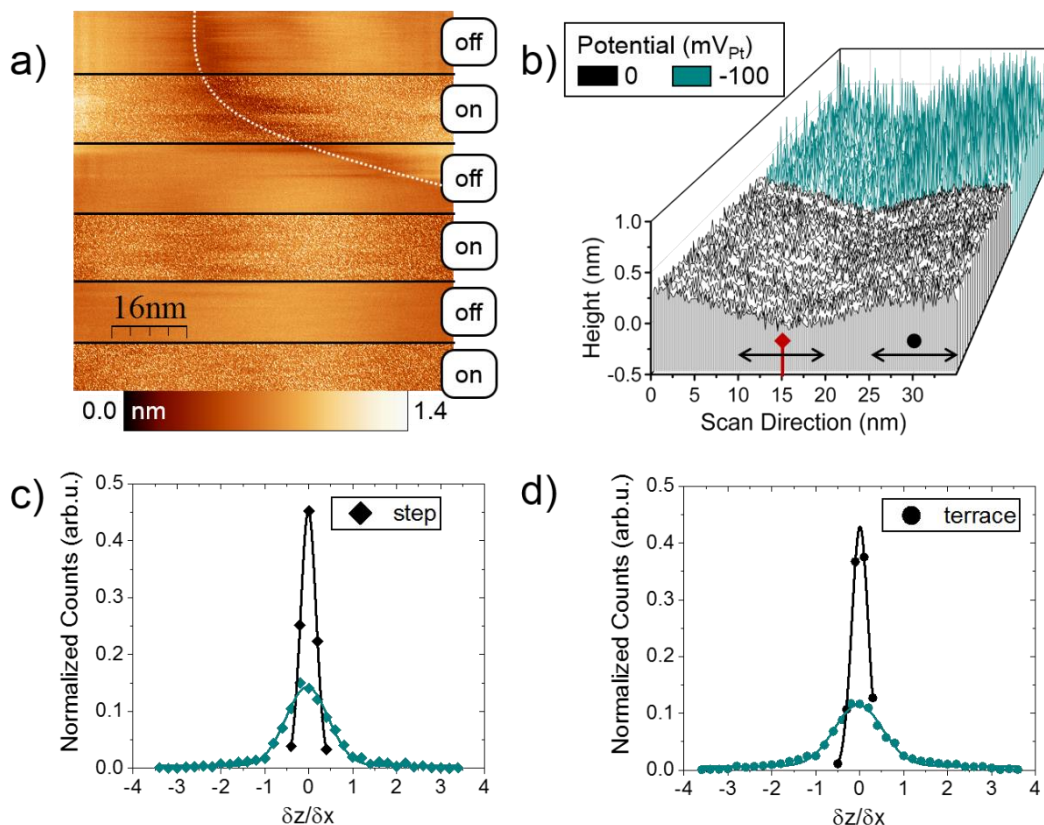
Figure 2. a) n-EC-STM measurement of a flat Pt$_3$Ni(111) surface containing a single step edge marked by a white line. When the reaction is turned "on", a considerable increase in the noise level is detected. The extent of the noise level suggests that terrace sites are as active as step sites. b) Line scans across the step edge in (a). The centre of the step is marked by a red diamond-shaped pin. c,d) Histograms of the signal derivatives for step and terrace sites (see main text for details). From the FWHM of the Gaussian fit, it can be assumed that terrace and step sites contribute comparably to the overall activity. Colour code: "off" (black), "on" (green). Note that the interatomic distance between Pt atoms is ca 0.27 nm.

Experiments on copper underpotential deposition and stripping (Figure S2) indicate that the surface of Pt$_3$Ni(111) in contact with the electrolyte indeed contains only Pt, as the charge of Cu stripping is close to the expected value for a Cu pseudomorphic overlayer on Pt (we note that Cu deposition is not possible on Ni atoms under these conditions for thermodynamic reasons).[58,59]

In the next step, n-EC-STM measurements were performed to determine the location of the active sites responsible for the enhanced ORR performance compared to pure Pt(111). Figure S3 illustrates the working principle of this technique.[13,14] In n-EC-STM, the electrolyte serves as a tunnelling medium. The sample potential can be varied such that a reaction at the electrode-electrolyte interface is enabled (reaction "on") or hindered (reaction "off"). When the reaction is turned "on", the noise level of the STM signal increases compared to reaction "off" if the tip is scanning over an active site. This is because the stability of the STM signal depends on the tunnelling barrier, which is governed by changes in the electrolyte,[60] species being adsorbed on the electrode surface,[61] and the movement of various species within the tunnelling gap.[62] We note that in this context "STM signal" refers either to tip-sample distance (height) or to the tunnelling current, depending on the chosen STM imaging mode. The distinct and confined noise level increase of the STM signal over the active sites can be exploited to in-situ locate them. An example of the high resolution of the technique is given in Figure S4, along with further details. To determine the sample potentials that can be assigned to reaction "on" and "off" conditions, a CV is recorded in the EC-STM setup versus the Pt quasi-reference electrode (Figure S3c). A potential of 0 mV$_{Pt}$ is chosen to correspond to the reaction "off" conditions as the respective measured overall sample current is approximately zero. For reaction "on", a negative potential was applied to the sample. Experimental parameters such as the potential for reaction "on", current set-point and tip potential are given in Table S2.

Figure 2a depicts an n-EC-STM measurement across the flat (111) surface containing a single step (marked with a white line). During the scan, the sample potential was alternated between 0 mV$_{Pt}$ ("off") and -100 mV$_{Pt}$ (ORR "on"). When the reaction is turned "on", a considerable increase in the noise level is observed compared to when no reaction takes place. The noise manifests itself as irregularly occurring values of high intensity in the STM signal, which can be seen as white dots in the STM image and spikes in the corresponding profile (line scans as given in Figure 2b). On the (111) terrace, the noise is homogeneously distributed,

indicating that the surface consists of equally active sites. Additional confirmation that terrace sites are homogenously active and show comparable noise levels, and thus similar activity, is included in Figure S5, where an n-EC-STM measurement was performed across a flat surface. In the region of the step edge, the noise seems to have the same extent as for terrace sites. In Figure 2b, line scans (height profile in scan direction) across the step are given for both reaction "on" and reaction "off". A diamond-shaped red pin marks the position of the step. It seems that the noise level (height and density of the spikes) is similar at step and terrace sites.

A semiquantitative approach helps strengthen the qualitative indications provided by the STM images.[14] First, the data were divided into step and terrace sites. The data points assigned to step sites were extracted from the centre of the step to a scan size of 5 nm in each direction. In the corresponding waterfall plot (Figure 2b), the position of the step is marked by the red diamond-shaped pin, and the arrow around the pin indicates the data attributed to the step sites. Another arrow marks the dataset for terrace sites, which was also confined to a width of 10 nm. Second, the STM signal (height z) was derived with respect to adjacent data points (in scan/x-direction) recorded during the scan ($\delta z/\delta x$). Third, histograms of these signal derivatives were rendered using a bin size (intervals in $\delta z/\delta x$-direction) of 0.2 for all images. To account for different sizes of datasets, the histograms are normalized to the number of data points taken for the respective dataset ("normalized counts"). Following the quantification approach reported previously,[14] the histograms were fitted by a Gaussian distribution, and the full width at half maximum (FWHM) was extracted to quantify the noise level.

The correlation between the FWHM and the noise level is the following: at low noise levels, there is not much signal distortion, and the corresponding histogram shows a narrow distribution with a small FWHM. Analogously, at high noise levels, the signal experiences distinct fluctuations and shows a broad histogram with a large FWHM. Figure 2c-d give the histograms for step and terrace sites, respectively, and compare reaction "off" (black) and "on" (green). If no reaction takes place, the histogram is narrow, which is indicative of a low noise level. Conversely, when the ORR is ongoing, the histogram broadens, corresponding to a high noise level. The FWHM and height of the Gaussian fit curve, which serve as a measure for the noise level, are listed in Table S3 for all n-EC-STM measurements. Interestingly, there is no significant difference in the noise level of steps and terraces under reaction conditions, suggesting that these sites are equally active.

To further relate the nature of active sites to the applied potential, additional n-EC-STM images were recorded. In Figure 3, two regular step edges of the (111) surface are visible. In the first part of the image, the reaction was switched "off", while the second part, recorded at -50 mV_{Pt}, marks the onset of the reaction (see CV in Figure S3c). In the following, the potential was lowered stepwise to -200 mV_{Pt}, which is equivalent to an increase in the ORR current. In the last part, the reaction was switched "off" to confirm the "reversibility" of the noise. We observe that the overall extent of the noise level is stronger with increasing "overpotential" in Figure 3a. The extent of the noise level is linked to the activity, which is comparable for step and terrace sites. This can be seen more easily in the corresponding line scans in Figure 3b, taken for the step on the left side. Line scans across the left step edge exclude the potential of -200 mV_{Pt} as it drifted out of the scan range.

Additionally, quantitative confirmation is given in the histograms in Figure 3c-d. For each applied potential, the FWHMs of step and terrace sites are comparable. Besides, it becomes apparent that the overall noise level increases with decreasing potential. This is understandable since an increased reaction rate leads to stronger fluctuations in the tunnelling medium and, thus, more signal noise.[14] Additional measurements are included in Figures S6 and S7. In Figure S6, step and terrace sites are comparably active, whereas in Figure S7 step sites are less active than terrace sites.

It is important to note that the appearance of a homogenous noise level on the Pt_3Ni(111) terraces, and the similar/equal noise level at the step sites are indeed due to a similar/equal activity and not caused by an insufficient resolution of the technique. In fact, the n-EC-STM method benefits from resolution in the nanometer regime. This was shown in previous works for active Pt step sites on a Pt(111) surface for the ORR (see also Figure S4),[13,14] studies of transition metal nanoislands on a support material,[13,42] and by the atomic resolution of active step and defect sites on carbon-based catalysts.[39,41] We emphasize again that the noise level in the measurements, which can be quantified in histograms as shown before, is directly proportional to the local activity. This correlation can be harnessed to extract useful electrocatalytic properties such as turnover frequencies and local onset potentials, capitalizing on a nanometre-scale resolution of n-EC-STM.[14,41,42]
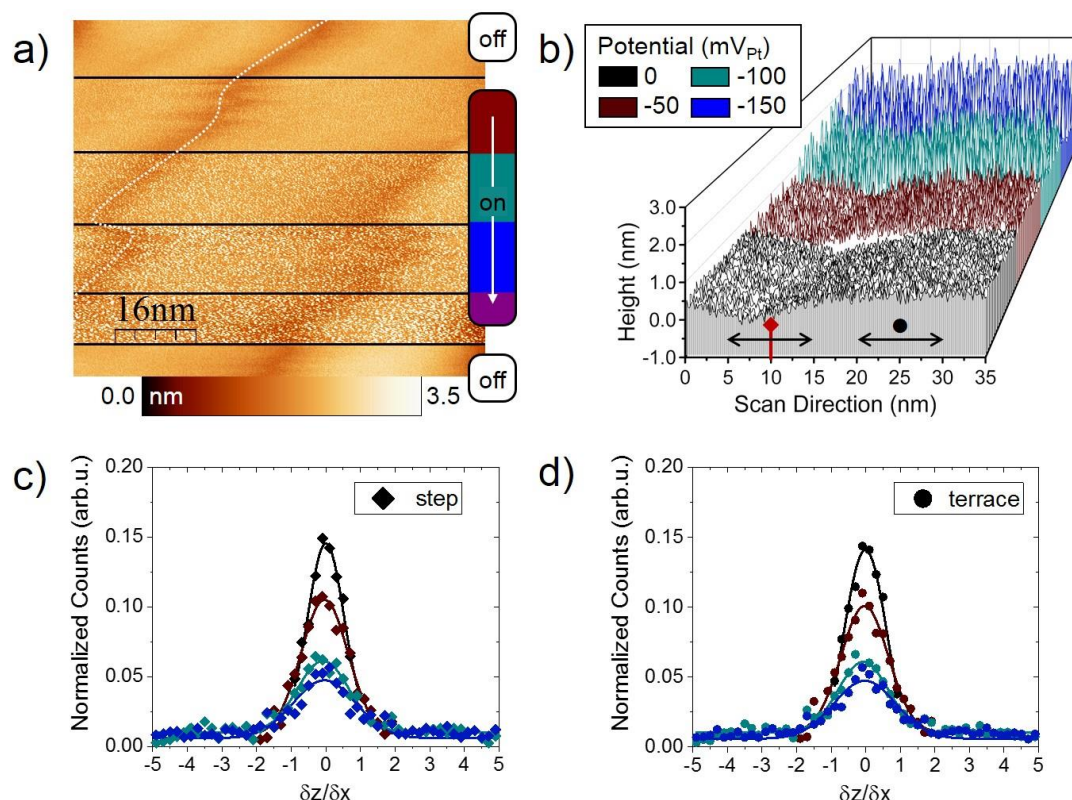
Figure 3. a) n-EC-STM measurement of two regular step edges on the Pt_3Ni(111) surface. During the recording of the image, the potential was varied according to the colour code. With decreasing potential (i.e. increasing ORR current), the noise features get more pronounced and a higher density of high-intensity spots is observed. The noise level of step and terrace sites seems comparable. b) Waterfall plot comprising the high profile in scan direction across the step marked in (a). From the data, histograms for the (c) step and (d) terrace sites were compiled. The histograms broaden and lose intensity with increasingly negative potential, suggesting a higher noise level. For each potential, the curves for step and terrace sites are comparable, suggesting their similar ORR activity.

Therefore, we conclude that the Pt₃Ni(111) surface consists solely of active sites, which is deduced from the homogeneous appearance of the recorded noise. The observation that the (111) facet is the most active among the low-index Pt₃Ni(hkl) surfaces was stated before[15] and used to synthesise high-performance octahedral Pt₃Ni particles.[63] It was explained by comparing the binding energy of *OH on Pt₃Ni(111) to Pt(111). Calculations show that an optimal ORR catalyst should bind *OH ~0.10 to 0.15 eV more weakly than Pt(111).[20,22] From experimental data (see also Tables S9-S10),[15] it was extracted that Pt₃Ni(111) binds *OH ~0.13-0.14 eV weaker than Pt(111).[57] This shows that the binding of intermediates is almost optimal on Pt₃Ni(111) surfaces, explaining why they are the most active areas.

Experimentally, the role of step sites in the catalytic process is difficult to evaluate. Hoshi et al. studied stepped Pt₃Ni(111) single crystals to probe the role of (111) and (100) step sites on the ORR activity.[53] They concluded that sites at or close to (100) steps are more active than (111) steps or regular (111) terraces. However, the authors concluded that from a macroscopic activity study of stepped single crystals, such that the role of the (111) terrace sites contributing to the overall measured activity can by
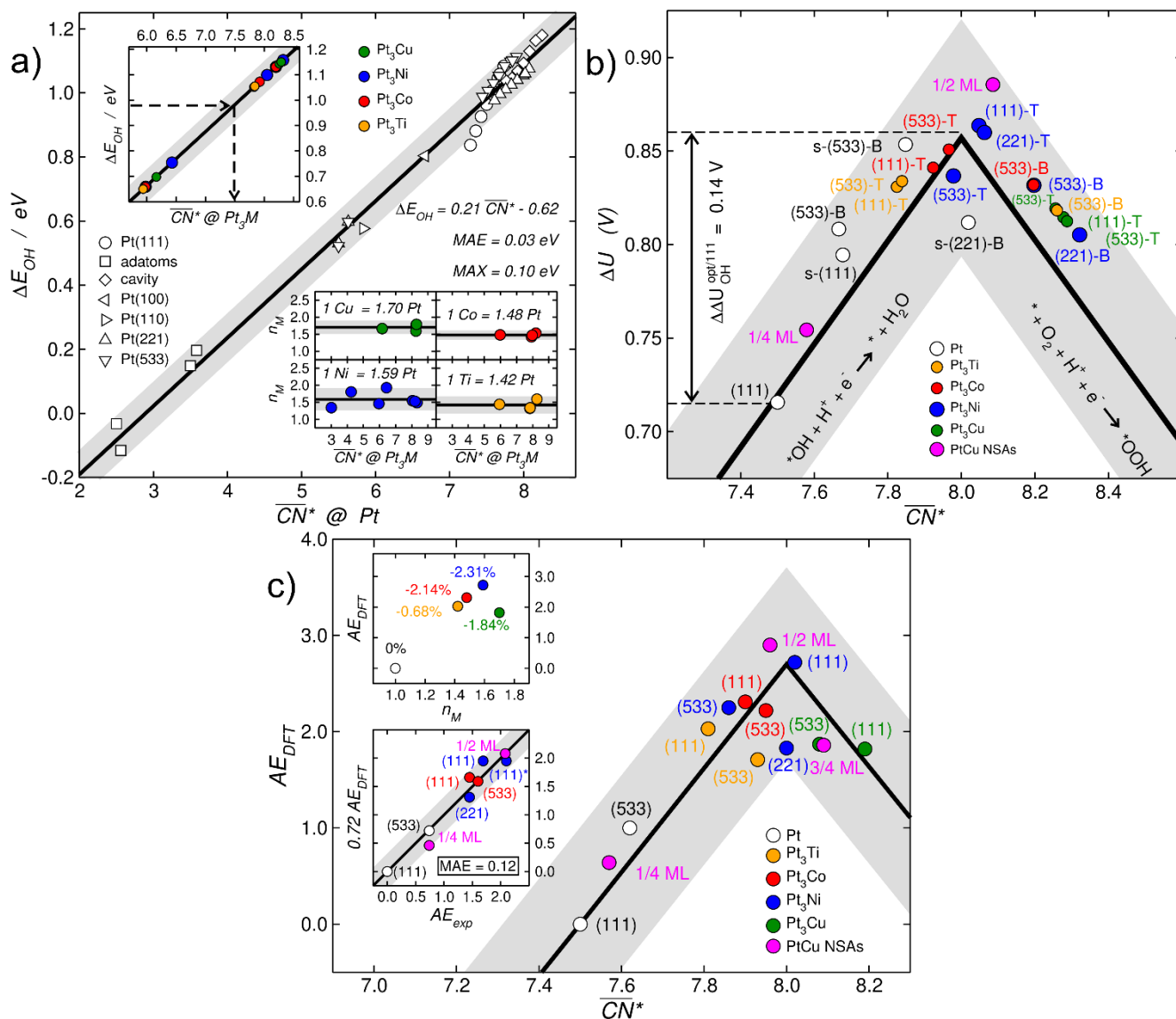
Figure 4. Computational modelling of the ORR on Pt-based electrocatalysts. a) DFT-calculated binding energies of *OH on a wide variety of pure Pt sites. The linear fit together with its associated mean and maximum absolute errors (MAE, MAX) are provided. The gray band around the linear fit corresponds to ± 2MAE. Top inset: assessment of the generalized coordination numbers of surface sites at Pt₃M (M = Ti, Co, Ni, Cu) using the correlation found in the main panel. The dashed lines indicate the procedure. Bottom insets: equivalence of M neighbours in terms of Pt neighbours (n_M) based on the generalized coordination numbers obtained in the top inset; see section S5.3. b) Coordination-activity plot for sites at pure Pt and Pt alloys. The most common potential-determining steps are shown on each side of the plot. The gray band around the black lines corresponds to ± 2MAE. T: terrace site, B: step-bottom site, s: strained site. The subsurface coverage of Cu in ML is provided for PtCu near-surface alloys. c) Activity enhancement (AE_{DFT}) with respect to Pt(111) as a function of a Boltzmann-weighted generalized coordination number of the electrodes, see sections S5.4-S5.5. Top inset: activity enhancement for Pt₃X(111) as a function of n_M. Lattice strain (%) is provided in each case. Bottom inset: comparison between experimental and calculated activity enhancements. Scaling the DFT-calculated enhancements by 0.72 renders a MAE of 0.12.

no means be neglected. In our study, which benefits from high resolution and is performed under reaction conditions, we observed step sites of less (Figure S6) and equal (Figure 2, Figure 3, and Figure S5) activity compared to terrace sites. Unfortunately, n-EC-STM is unable to ascertain the orientation of the step edges. With these observations in mind, we assume that the highly active step edges are presumably oriented in a (100) fashion, whereas the less active steps may be (111)-oriented. To compensate for this inherent drawback of the technique and reach a more thorough assessment of the nature of active sites on $Pt_3Ni(111)$ and akin alloys, we resort to a structure-sensitive computational electrocatalysis model, which is introduced in the following.

The simplest geometric descriptor for active sites at pure metal surfaces is the coordination number (cn), which is a count of the nearest neighbours around the active site, assuming that all neighbours are identical and equivalent to those in the bulk of the material. A first-order extension called "generalized coordination number" ($\overline{CN}$) allows distinguishing between inequivalent nearest neighbours by considering the second-nearest neighbours in the count.[22,64] In doing so, it is feasible to capture finite-size effects and directly compare sites at nanoparticles and extended surfaces, and make activity predictions.[65,66] Moreover, compressive and tensile strain can be incorporated in simple terms into generalized coordination numbers (denoted as $\overline{CN}^*$).[50] However, neither the conventional nor the generalized coordination numbers are suitable for alloys, in which ligand effects are present, often in combination with strain effects. So far, this has prevented the elaboration of a unified geometric picture for alloys and pure metals and motivated the elaboration of more sophisticated analyses.[67,68,69]

A step forward is taken in Figure 4a, which provides a simple method for incorporating alloying effects into $\overline{CN}^*$. First, a calibration curve with mean and maximum absolute errors close to chemical accuracy (MAE = 0.03 eV, MAX = 0.10 eV) is made based on *OH binding energies and $\overline{CN}^*$ for pure Pt sites. Subsequently, the curve is used to estimate the $\overline{CN}^*$ of sites at Pt_3M alloys (M = Cu, Ni, Co, Ti), as shown in the top inset of Figure 4a. From the difference between those numbers and the values obtained for analogous pure Pt sites, it is possible to calculate the equivalence of an M neighbour in terms of Pt neighbours (denoted n_M in the bottom inset of Figure 4a, see section S6.3). On average, we find that Cu, Ni, Co and Ti atoms are equivalent to 1.70 ± 0.12, 1.59 ± 0.25, 1.48 ± 0.05, 1.42 ± 0.17 Pt atoms, respectively (n_M in Figure 4a, bottom inset, see also Table S5. The ranges include in each case at least 85% of the analysed data). These values can be used to assess the $\overline{CN}^*$ on all sorts of geometric sites on Pt_3M alloys with the topmost layer consisting only of Pt atoms.

To illustrate the assessment of the alloy-sensitive $\overline{CN}^*$, we consider the example of $Pt_3Ni(111)$ terraces. Their *OH binding energy is 1.10 eV which, according to the regression in Figure 4a, corresponds to $\overline{CN}^* = 8.05$. This differs from the value of pristine Pt(111) terraces ($\overline{CN}^* = 7.5$) by 0.55 coordination units, such that a Ni neighbour in the second layer is equivalent to 1.55 Pt neighbours (see Table S5). By averaging over several different sites, we arrived at the value of 1 Ni = 1.59 ± 0.25 Pt atoms for Pt_3Ni (Figure 4a, bottom inset). In the SI, section S6.3, the procedure is shown in detail, and the values are tabulated for all Pt_3M sites under study. For PtCu NSAs, the procedure is analogous, except that the subsurface Cu coverage and the number of Cu neighbours around the active sites need to be considered. Once the $\overline{CN}^*$ of the alloy sites are known, their ORR activities can be predicted with the coordination-activity plot in Figure 4b, which correlates the ORR limiting potential (ΔU) and the generalized coordination of the active sites.[22,50]

The findings listed below support our experimental results and past activity measurements on bulk single crystals.[26,53,70] Furthermore, they provide insight that goes beyond such reports:

- $Pt_3Ni(111)$ terraces (blue (111)-T in Figure 4b) are the most active sites, while some terrace sites near step edges are close in activity (e.g. blue (221)-T), and step-bottom sites are less active (e.g. blue (221)-B).
- Although $Pt_3Co(111)$ terraces (red (111)-T) are considerably more active than Pt(111), they are less active than $Pt_3Ni(111)$ terraces.
- Pt sites strained as much as in Pt_3Ni (s = -2.31%) but with no Ni neighbours are more active than Pt(111); depending on the geometry of the active site, they can be more or less active than sites with Ni neighbours. In particular, the limiting potential of step-bottom sites at strained Pt(533) (s-(533)-B) is similar to that of $Pt_3Ni(111)$ terraces (blue (111)-T), suggesting that strained step-bottom areas with low or no Ni content can be rather active for the ORR.
- NSAs of Pt and submonolayer amounts of Cu are more active than Pt(111), and 0.5 ML Cu in the subsurface render (111) terrace sites more active than $Pt_3Ni(111)$ terraces because of ligand effects.
- As a general trend, step-edge sites on pure and alloyed Pt surfaces are rather undercoordinated ($\overline{CN}^* \approx 6.0$), bind *OH strongly, and hence display low ORR activities, see section S5.3.

It is possible to go beyond the coordination-activity plot to predict the relative activity of the catalysts by virtue of the individual contributions of their active sites. This is done in Figure 4c, where we correlate the Boltzmann-weighted $\overline{CN}^*$ of several Pt-based electrocatalysts and their activity enhancement (AE) with respect to Pt(111) using a simplified version of the Butler-Volmer equation, see section S6.4 of the SI. Figure 4c confirms that $Pt_3Ni(111)$ is close to the top of the volcano and that step edges (as

found in Pt$_3$Ni(221) and Pt$_3$Ni(533)) lower the activity. Nonetheless, the enhancement of all Pt$_3$Ni alloys compared to Pt(111) is substantial. Pt$_3$Co(111) is less active than Pt$_3$Ni(111) and (100) steps render slightly less active alloy surfaces. Pt$_3$Ti is less active than Pt$_3$Co and Pt$_3$Ni, which has been verified experimentally for polycrystalline electrodes.[21] Finally, steps do not seem to modify the activity of Pt$_3$Cu, but ligand effects substantially modify the activity of PtCu NSA electrodes. In particular, PtCu(111) NSAs with a subsurface coverage of 0.5 ML Cu surpass the activity of Pt$_3$Ni(111), in line with experiments.[26]

The top inset of Figure 4c shows how the interplay of ligand and strain effects (described by n_M and the percentage of lattice compression) grant Pt$_3$Ni(111) the largest activity enhancement among the analysed Pt$_3$M(111) alloys. Finally, the results are compared to experimental data in the bottom inset of Figure 4c. We note that DFT models tend to overestimate electrocatalytic activities, in particular around the volcano apex.[36] For instance, the highest reported activity enhancement in our dataset is that of PtCu NSAs with 0.5 ML Cu (AE_{exp} = 2.08),[26] which is equivalent to 72% of the calculated one. We used that number as a scale factor for all other electrodes, including data for pure Pt, Pt$_3$Ni, Pt$_3$Co and PtCu NSAs, and found that the mean absolute error is only 0.12. The agreement between theory and experiments upon scaling suggests that the terms neglected in our simplified Butler-Volmer model do not alter the trends and are relatively constant among Pt-based alloys. One such term might be the solvent reorganization energy. Details on the assessment of AE_{DFT} and specific values can be found in sections S6.4 and S6.5.

In sum, Figure 4 explains that a suitable interplay of strain and ligand effects can push a Pt-based material toward the ORR activity optimum, and opens the path toward the computational design of electrocatalytically active sites with both structural and compositional predictiveness.

Conclusion

We applied n-EC-STM on a Pt$_3$Ni(111) single-crystal electrode to identify the active sites towards the ORR in acid. We found that the most active sites are located on the basal plane of Pt$_3$Ni(111), in contrast to pure Pt, where they are located at concave sites close to the steps. Here, a homogenously increased noise level suggests that all sites are equally active. Step sites were found to be either slightly less or similarly active compared to terraces. Furthermore, we devised alloy-sensitive generalized coordination numbers and created site-specific and material-specific ORR activity plots. We were able to assess how much Co, Ni and Cu increase the generalized coordination of Pt surface sites by virtue of strain and/or ligand effects. We observed that the combination of such effects is nearly optimal in Pt$_3$Ni(111), insufficient to reach the top of the activity plot for Pt$_3$Co(111) and Pt$_3$Ti(111), and unnecessarily large for Pt$_3$Cu. Ligand effects in PtCu NSAs also enhance the activity with respect to pure Pt depending on the subsurface Cu coverage. With this report, we expand the current knowledge and design principles of active sites for the ORR from pure Pt to Pt alloys in acidic medium. We anticipate that the interplay of experimental and computational tools shown here is useful to outline the structure and composition of the active sites for numerous other alloys and electrocatalytic reactions.

Author contributions

The manuscript was written through contributions of all authors. All authors approved the final version of the manuscript.

Conflicts of interest

There are no conflicts to declare.

Acknowledgements

References

1   A.S. Arico, P. Bruce, B. Scrosati, J.M. Tarascon, W. van Schalkwijk, *Nature Mater.*, 2005, **4**, 366-377.

2   W.T. Yu, M.D. Porosoff, J.G.G. Chen, *Chem. Rev.*, 2012, **112**, 5780-5817.

3   K. Sasaki, H. Naohara, Y. Choi, Y. Cai, W. Chen, P. Liu, R.R. Adzic, *Nature Commun.*, 2012, **3**, 1-5.

4   A. Kulkarni, S. Siahrostami, A. Patel, J. K. Nørskov, *Chem. Rev.*, 2018, **118**, 2302–2312

5   Z. W. Seh, J. Kibsgaard, C. F. Dickens, I. Chorkendorff, J. K. Nørskov, T. F. Jaramillo, *Science*, 2017*, **355**, eaad4998.

6   J. K. Nørskov, J. Rossmeisl, A. Logadottir, L. Lindqvist, J. R. Kitchin, T. Bligaard, H.J. Jónsson, *Phys. Chem. B*, 2004, **108**, 17886-17892.

7   N. M. Marković, P.N. Ross, *Surf. Sci. Rep.*, 2002, **45**, 117-229.

8   A. S. Bandarenka, M.T.M. Koper, *J. Catal.*, 2013, **308**, 11-24.

9   R. Rizo, E. Herrero, J.M. Feliu, *Phys. Chem. Chem. Phys.*, 2013, **15**, 15416-15425.

10 A. Hitotsuyanagi, M. Nakamura, N. Hoshi, *Electrochim. Acta*, 2012, **82**, 512-516.

11 A. Kuzume, E. Herrero, J. M. Feliu, *J. Electroanal. Chem.*, 2007, **599**, 333-343.

12 F. Calle-Vallejo, M. D. Pohl, D. Reinisch, D. Loffreda, P. Sautet, A. S. Bandarenka, *Chem. Sci.*, 2017, **8**, 2283-2289.

13 J. H. Pfisterer, Y. Liang, O. Schneider, A. S. Bandarenka, *Nature*, 2017, **549**, 74–77.

14 R. W. Haid, R. M. Kluge, Y. Liang, A. S. Bandarenka, *Small Methods*, 2020, **4**, 2000710.

15 V.R. Stamenković, B. Fowler, B. S. Mun, G. Wang, P.N. Ross, C. A. Lucas, N. M. Marković, *Science*, 2007, **315**, 493-497.

16 C. Chen, Y. Kang, Z. Huo, Z. Zhu, W. Huang, H. L. Xin, J. D. Snyder, D. Li, J. A. Herron, M. Mavrikakis, M. Chi, K. L. More, Y. Li, N. M. Marković, G. A. Somorjai, P. Yang, V. R. Stamenković, *Science*, 2014, **343**, 1339-1343.

17 J. Kibsgaard, Y. Gorlin, Z. Chen, T. F. Jaramillo, *J. Am. Chem. Soc.*, 2012, **134**, 7758-7765.

18 R. Chattot, T. Asset, P. Bordet, J. Drnec, L. Dubau, F. Maillard, *ACS Catal.*, 2017, **7**, 398–408.

19 J. Fichtner, S. Watzele, B. Garlyyev, R.M. Kluge, F. Haimerl, H.A. El-Sayed, W. Li, F.M. Maillard, L. Dubau, R. Chattot, J. Michalička, J. M. Macak, W. Wang, D. Wang, T. Gigl, C. Hugenschmidt, A. S. Bandarenka, *ACS Catal.*, 2020, **10**, 3131-3142.

20 J. Greeley, I.E.L Stephens, A.S. Bondarenko, T.P. Johansson, H.A. Hansen, T.F. Jaramillo, J. Rossmeisl, I. Chorkendorff, J.K. Nørskov, *Nat. Chem.*, 2009, **1**, 552–556.

21 V.R. Stamenković, B.S. Mun, K.J.J. Mayrhofer, P.N. Ross, N.M. Marković, J. Rossmeisl, J. Greeley, J.K. Nørskov, *Angew. Chem. Int. Ed.*, 2006, **45**, 2897–2901.

22 F. Calle-Vallejo, J. Tymoczko, V. Colic, Q. Huy Vu, M. D. Pohl, K. Morgenstern, D. Loffreda, P. Sautet, W. Schuhmann, A. S. Bandarenka, *Science*, 2015, **350**, 185-189.

23 M. Escudero-Escribano, P. Malacrida, M. H. Hansen, U. G. Vej-Hansen, A. Velázquez-Palenzuela, V. Tripkovic, J. Schiøtz, J. Rossmeisl, I. E. L. Stephens, I. Chorkendorff, *Science*, 2016, **352**, 73-76.

24 M. Liu, Z. Zhao, X. Duan, Y. Huang, *Adv. Mater.*, 2019, **31**, 1802234.

25 J. Fichtner, B. Garlyyev, S. Watzele, H.A. El-Sayed, J.N. Schwämmlein, W. Li, F.M. Maillard, L. Dubau, J. Michalička, J.M. Macak, A. Holleitner, A.S. Bandarenka, *ACS Appl. Mater. Interfaces*, 2019, **11**, 5129-5135.

26 I. E. L. Stephens, A. S. Bondarenko, F. J. Perez-Alonso, F. Calle-Vallejo, L. Bech, T. P. Johansson, A. K. Jepsen, R. Frydendal, B. P. Knudsen, J. Rossmeisl, I. Chorkendorff, *J. Am. Chem. Soc.*, 2011, **133**, 5485–5491.

27 F. Calle-Vallejo, M. T. M. Koper, A. S. Bandarenka, *Chem. Soc. Rev.*, 2013, **42**, 5210-5230.

28 L. Gan, C. Cui, M. Heggen, F. Dionigi, S. Rudi, P. Strasser, *Science*, 2014, **346**, 1502–1506.

29 M. Escudero-Escribano, A. Verdaguer-Casadevall, P. Malacrida, U. Grønbjerg, B. P. Knudsen, A. K. Jepsen, J. Rossmeisl, I. E. Stephens, I. Chorkendorff, *J. Am. Chem. Soc.*, 2012, **134**, 16476-16479.

30 S. Mi, N. Cheng, H. Jiang, C. Li, H. Jiang, *RSC Adv.*, 2018, **8**, 15344-15351.

31 X. Tian, X. Zhao, Y. Su, L. Wang, H. Wang, D. Dang, B. Chi, H. Liu, E.J.M. Hensen, X.W. Lou, B.Y. Xia, *Science*, 2019, **366**, 850-856.

32 Y.-J. Wang, N. Zhao, B. Fang, H. Li, X.T. Bi, H. Wang, H., *Chem. Rev.*, 2015, **115**, 3433-3467.

33 F. Maroun, F. Ozanam, O. M. Magnussen, R. J. Behm, *Science*, 2001, **293**, 1811-1814.

34 J. R. Kitchin, J. K. Nørskov, M. A. Barteau, J. G. Chen*, J. Chem. Phys.*, 2015, **120**, 10240-10246.

35 Q. Jia, W. Liang, M.K. Bates, P. Mani, W. Lee, S. Mukerjee, *ACS Nano*, 2015, **9**, 387-400.

36 I. E. L. Stephens, A.S. Bondarenko, U. Gronbjerg, J. Rossmeisl, I. Chorkendorff, *Energy Environ. Sci.*, 2012, **5**, 6744-6762.

37 C. Wang, M. Chi, D. Li, D. Strmcnik, D. van der Vliet, G. Wang, V. Komanicky, K.-C. Chang, A.P. Paulikas, D. Tripkovic, *J. Am. Chem. Soc.*, 2011, **133**, 14396-14403.

38 R. M. Kluge, R. W. Haid, A. S. Bandarenka, *J. Catal.*, 2021, **396**, 14-22.

39 R. M. Kluge, R. W. Haid, I. E. L. Stephens, F. Calle-Vallejo, A. S. Bandarenka, *Phys. Chem. Chem. Phys.*, 2021, **23**, 10051-10058.

40 R. M. Kluge, E. Psaltis, R. W. Haid, S. Hou, T. O. Schmidt, O. Schneider, B. Garlyyev, F. Calle-Vallejo, A. S. Bandarenka, *ACS Appl. Mater. Interfaces*, 2022, **14**, 19604.

41 T. Kosmala, A. Baby, M. Lunardon, D. Perilli, H. Liu, C. Durante, A. Di Valentin, S. Agnoli, G. Granozzi, *Nat. Catal.*, 2021, **4**, 850–859.

42 M. Lunardon, T. Kosmala, C. Durante, S. Agnoli, G. Granozzi, *Joule*, accepted. http://dx.doi.org/10.2139/ssrn.3974120

43 I. Horcas, R. Fernández, J. M. Gómez-Rodríguez, J. Colchero, J. Gómez-Herrero, A. M. Baro, *Rev Sci Instrum.*, 2007, **78**, 013705.

44 T. J. Schmidt, H. A. Gasteiger, G. D. Stab, P. M. Urban, D. M. Kolb, R. J. Behm, *J. Electrochem. Soc.*, 1998, **145**, 2354-2358.

45 L. A. Nagahara, T. Thundat, S. M. Lindsay, *Rev. Sci. Instrum.*, 1989, **60**, 3128-3130.

46 G. Kresse, J. Furthmüller, *Phys. Rev. B*, 1996, **54**, 11169-11186.

47 J. P. Perdew, K. Burke, M. Ernzerhof, *Phys. Rev. Lett.*, 1996, **77**, 3865-3868

48 G. Kresse, D. Joubert, *Phys. Rev. B*, 1999, **59**, 1758-1775.

49 H. J. Monkhorst, J. D. Pack, *Phys. Rev. B*, 1976, **13**, 5188-5192.

50 F. Calle-Vallejo, A. S. Bandarenka, *ChemSusChem,* 2018, **11**, 1824 –1828.

51 Z.-D. He, S. Hanselman, Y.-X. Chen, M. T. M. Koper, F. Calle-Vallejo, *J. Phys. Chem. Lett.*, 2017, **8**, 2243–2246.

52 J. Kim, W. H. Doh, H. Kondoh, K. Mase, J.-J. Gallet, F. Bournel, B. S. Mun, J. Y. Park, *J. Electron Spectrosc. Relat. Phenom.*, 2020, **238**, 146857.

53 T. Rurigaki, A. Hitotsuyanagi, M. Nakamura, N. Sakai, N. Hoshi, *J. Electroanal. Chem.*, 2014, **716**, 58-62.

54 P. Strasser, S. Koh, T. Anniyev, J. Greeley, K. Moore, C. Yu, Z. Liu, S. Kaya, D. Nordlund, H. Ogasawara, M.F. Toney, A. Nilsson, *Nat. Chem.*, 2010, **2**, 454-460.

55 Z. Duan, G. Wang, *Phys. Chem. Chem. Phys.*, 2011, **13**, 20178–20187.

56 S. Kattel, G. Wang, *J. Chem. Phys.*, **2014**, 141, 124713.

57 V. Čolić, A.S. Bandarenka, ACS Catal., 2016, 6, 5378-5385.

58 I. E. L. Stephens, A. S. Bondarenko, L. Bech, I. Chorkendorff, *ChemCatChem*, 2012, **4**, 341–349.

59 B. Garlyyev, M. D. Pohl, V. Čolić, Y. Liang, F. K. Butt, A. Holleitner, A. S. Bandarenka, *Electrochem. Commun*., 2018, **88**, 10–14.

60 M. Hugelmann, W. Schindler, *Surface Sci.*, 2003, **541**, L643-L648.

61 M. Sumetskii, A. A. Kornyshev, U. Stimming, *Surf. Sci.*, 1994, **307**, 23-27.

62 M. Sumetskii, A. A. Kornyshev, *Phys. Rev. B*, 1993, **48**, 17493-17506.

63 J. Zhang, H. Z. Yang, J. Y. Fang, S. Z. Zou, *Nano Lett.*, 2010, **10**, 638-644.

64 F. Calle-Vallejo, J. I. Martínez, J. M. García-Lastra, P. Sautet, D. Loffreda, *Angew. Chem. Int. Ed.*, 2014, **53**, 8316-8319.

65 K. Rossi, G. G. Asara, F. Baletto, *Phys. Chem. Chem. Phys.,* 2019, **21**, 4888-4898.

66 M. Rück, A. S. Bandarenka, F. Calle-Vallejo, A. Gagliardi, *J. Phys. Chem. Lett.*, 2018, **9**, 4463–4468.

67 X. Ma, H. Xin, *Phys. Rev. Lett.*, 2017, **118**, 036101.

68 T. S. Choksi, L. T. Roling, V. Streibel, F. Abild-Pedersen, *J. Phys. Chem. Lett.*, 2019, **10**, 1852–1859.

69 L. T. Roling, T. S. Choksi, F. Abild-Pedersen, *Nanoscale*, 2019, **11**, 4438-4452.

70 Y. Takesue, M. Nakamura, N. Hoshi, *Phys. Chem. Chem. Phys*., 2014, **16**, 13774-13779.